Article

Sunlight-Driven Photothermally Boosted Photocatalytic Eradication of Superbugs Using a Plasmonic Gold Nanoparticle-Decorated WO₃ Nanowire-Based Heterojunction

Avijit Pramanik, Shivangee Rai, Kaelin Gates, Olorunsola Praise Kolawole, Sanchita Kundu,
Pragathi Kasani-Akula, Jagriti Singh, Jerusha Dasary, Huimin Zhang, Fengxiang X. Han,
and Paresh Chandra Ray*

Read Online

ACCESS | Metrics & More | Article Recommendations | Supporting Information

ABSTRACT: Superbug infections are currently one of the biggest global health problems in our society. Herein, we report the design of a plasmonic gold nanoparticle (GNP)-decorated WO₃ nanowire-based heterojunction for the proficient usage of sunlight-based renewable energy to inactivate 100% superbugs via photothermally boosted photocatalytic action. Additionally, a synergistic photothermal and photocatalytic approach has been used for sunlight-driven complete eradication of carbapenem-resistant Enterobacteriaceae *Escherichia coli* (CRE *E. coli*) and methicillin-resistant *Staphylococcus aureus* (MRSA) superbugs. Interestingly, photocatalytic activity of methylene blue (MB) dye degradation in the presence of 670 nm near-infrared light shows that photothermally boosted photocatalytic performance is much superior to that of only a photocatalytic or photothermal process. The observed higher photocatalytic performance for the heterojunction is because the plasmonic GNP enhanced the absorption capability at 670 nm and increased the temperature of the photocatalyst surface, which reduces the activation energy of the degradation reaction. Similarly, sunlight-driven photocatalytic experiments show 100% degradation of MB after 60 min of sunlight irradiation. Moreover, sunlight-based photocatalytic inactivation of MRSA and CRE *E. coli* experiments show 100% inactivation after 60 min of light irradiation.
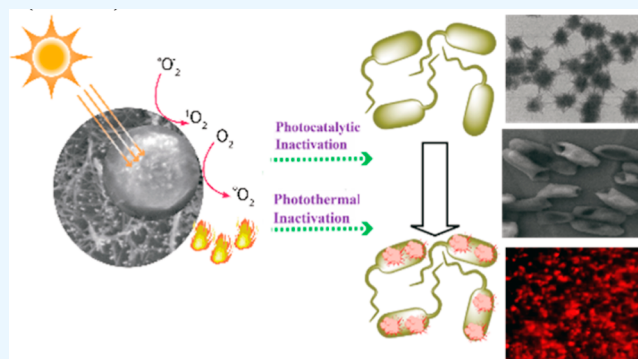
1. INTRODUCTION

Pathogenic bacteria resistant to currently available antibiotics in the market have emerged as a serious concern to the global public health.[1−8,19,47] According to the World Health Organization (WHO), superbugs or multiple drug-resistant pathogenic bacterial infections are responsible for more than 4.95 million deaths every year.[1] As per the United Nations, if antibiotic abuse continues at the same rate, superbug infections will be responsible for more than 10 million/year deaths by 2050.[2−8,19,47] Moreover, superbugs are becoming resistant to a new type of antibiotic faster than the antibiotics established in clinics, and as a result, no new class of antibiotics has been in the market in the last 30 years.[9−16,30,46]

Since in the 21st century, superbug infection is one of the biggest battles in global health, the development of innovative antisuperbug agents that do not cause drug resistance is extremely important to save lives.[17−31,41] Driven by the need of our society, in the current article, we report the design of a sunlight-driven photothermal−photocatalytic heterojunction using plasmonic gold nanoparticle (GNP)-decorated WO₃ nanowires for complete eradication of carbapenem-resistant

Enterobacteriaceae *Escherichia coli* (CRE *E. coli*) and methicillin-resistant *Staphylococcus aureus* (MRSA) superbugs as shown in Figure 1. Since sunlight is a renewable energy source that is the most efficient and easily available, developing a sunlight-based catalyst for inactivation of superbugs will have huge implications for our society.[2−7,47]

Moreover, sunlight energy, which reaches the ground of this earth, consists of ∼4% ultraviolet light (<400 nm), ∼43% visible light (400−650 nm), and 53% near-infrared (NIR) (>650 nm).[2−8,19,47] As a result, the development of a new catalyst that has strong absorption in visible and NIR regions will be highly effective for the inactivation of superbugs using sunlight.[9−16,30,46]
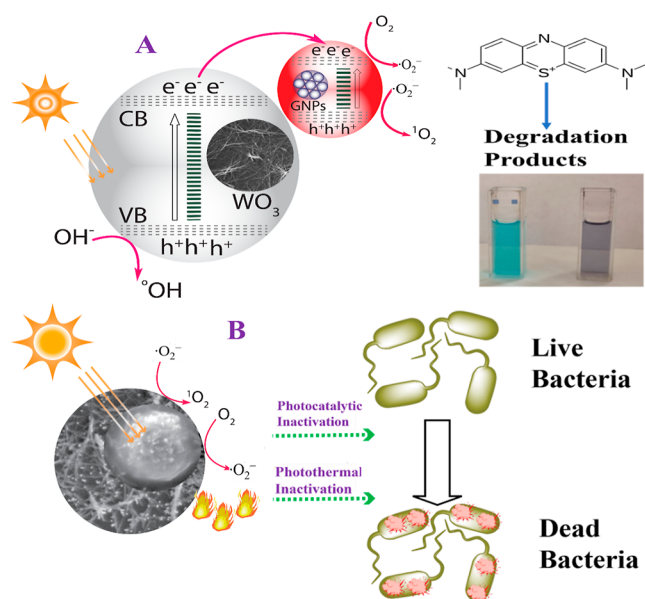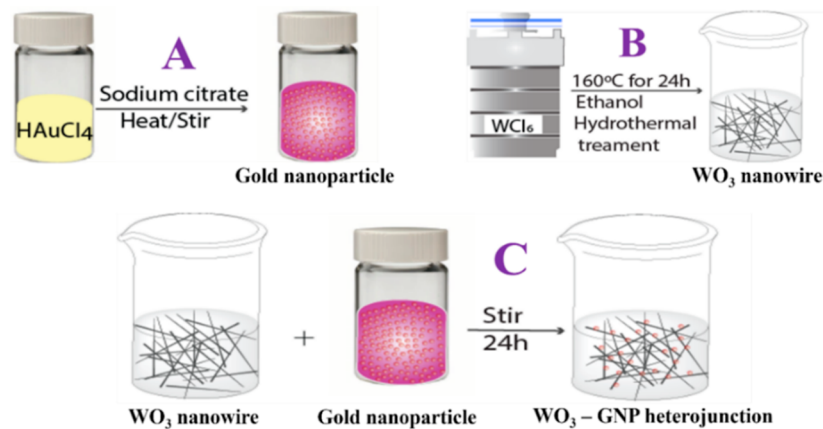
Figure 1. (A) Schematic representation shows the possible pathway for the sunlight-driven photothermally boosted photocatalytic degradation of MB dye using a plasmonic GNP-decorated WO_3 nanowire-based heterojunction catalyst. (B) Schematic representation shows the possible pathway for the sunlight-driven photothermally boosted photocatalytic inactivation of superbugs using a plasmonic GNP-decorated WO_3 nanowire-based heterojunction catalyst.

Recently, photothermal and photocatalytic agents used for killing pathogens have become promising strategies for the treatment of antibiotic-resistant pathogens.[36−51] In the case of photocatalytic agents, the reactive oxygen species (ROS) produced in the presence of light can effectively degrade superbugs.[36−51] In the presence of light, the dipole of a photocatalytic system interacts with the electric field of the light, which generate holes (h^+) in the valence bond and electrons ($e^−$) in the conductance band.[25−40] Next, due to the strong oxidizing abilities of holes, the h^+ helps form hydroxy radicals ($^\bullet OH$),[16−30,41] as shown in Figure 1. On the other hand, due to the strong reducing abilities of electrons, $e^−$ helps form the superoxide radical ($^\bullet O_2^−$) and singlet oxygen ($^1O_2$),[12−25,41,46] as shown in Figure 1. It is now well documented that WO_3-based nanomaterials are indirect band

gap semiconductor material, with a band gap of 2.8 eV, and can generate electron−hole pairs in the presence of UV light.[17−30,41] However, WO_3-based nanomaterials exhibit lower photocatalytic efficiency under sunlight, which is due to the lack of good absorption in the visible and NIR regions; as a result, sunlight cannot be used in full capacity to produce ROS when WO_3-based nanomaterials have been used as photocatalysts.[35−45]

To overcome this, we have designed a heterojunction using a plasmonic GNP-decorated WO_3 nanowire. In our design of the heterojunction photocatalyst, the localized surface plasmon resonance (SPR) of the plasmonic GNP has been utilized to enhance the light−matter interactions in the visible and NIR regions.[25−35] So, the GNP has been used to enhance the photocatalytic performance of the WO_3 nanowire via enhancing visible and NIR light absorption, which allow us to use sunlight in full capacity to produce ROS. Similarly, it is also now well documented that the photocatalytic efficiency of WO_3 nanomaterials is significantly low, which is due to the high degree of the recombination process between holes (h^+) and electrons ($e^−$) pairs.[25−35] The recombination process between $e^−$ and h^+ restricts WO_3 to be used in full capacity to produce ROS, which is the most important step for the photocatalytic process.[25−35] To overcome this, we have designed a heterojunction using a plasmonic GNP-decorated WO_3 nanorod. In our design of the heterojunction photo-catalyst, the plasmonic GNP has been utilized to decrease the recombination process between electrons and holes for photoexcited WO_3.[29−39]

The Schottky barrier formed at the WO_3/GNP interface can facilitate the separation of photogenerated carriers and thus suppresses the detrimental recombination process,[8−16,30,46] as shown in Figure 1. Similarly, GNPs have the capability of converting light energy into thermal energy, which can degrade superbugs via a hyperthermia process.[40−51] The photothermal effect of the GNP can enhance the local temperature of the WO_3 photocatalyst surface, which can reduce the activation energy of the reaction and improve the charge separation efficiency.[40−51] Reported data show that the heterojunction can destroy 100% CRE *E. coli* and MRSA superbugs within 20 min of 670 nm light exposure via a photothermally boosted photocatalytic mechanism.

Figure 2. Schematic representation shows the design steps we have used for the synthesis of the spherical GNP-decorated WO_3 nanowire-based heterojunction. (A) Synthesis of spherical GNPs. (B) Solvothermal synthesis of WO_3 nanowires. (C) Development of the GNP-decorated WO_3 nanowire-based heterojunction.
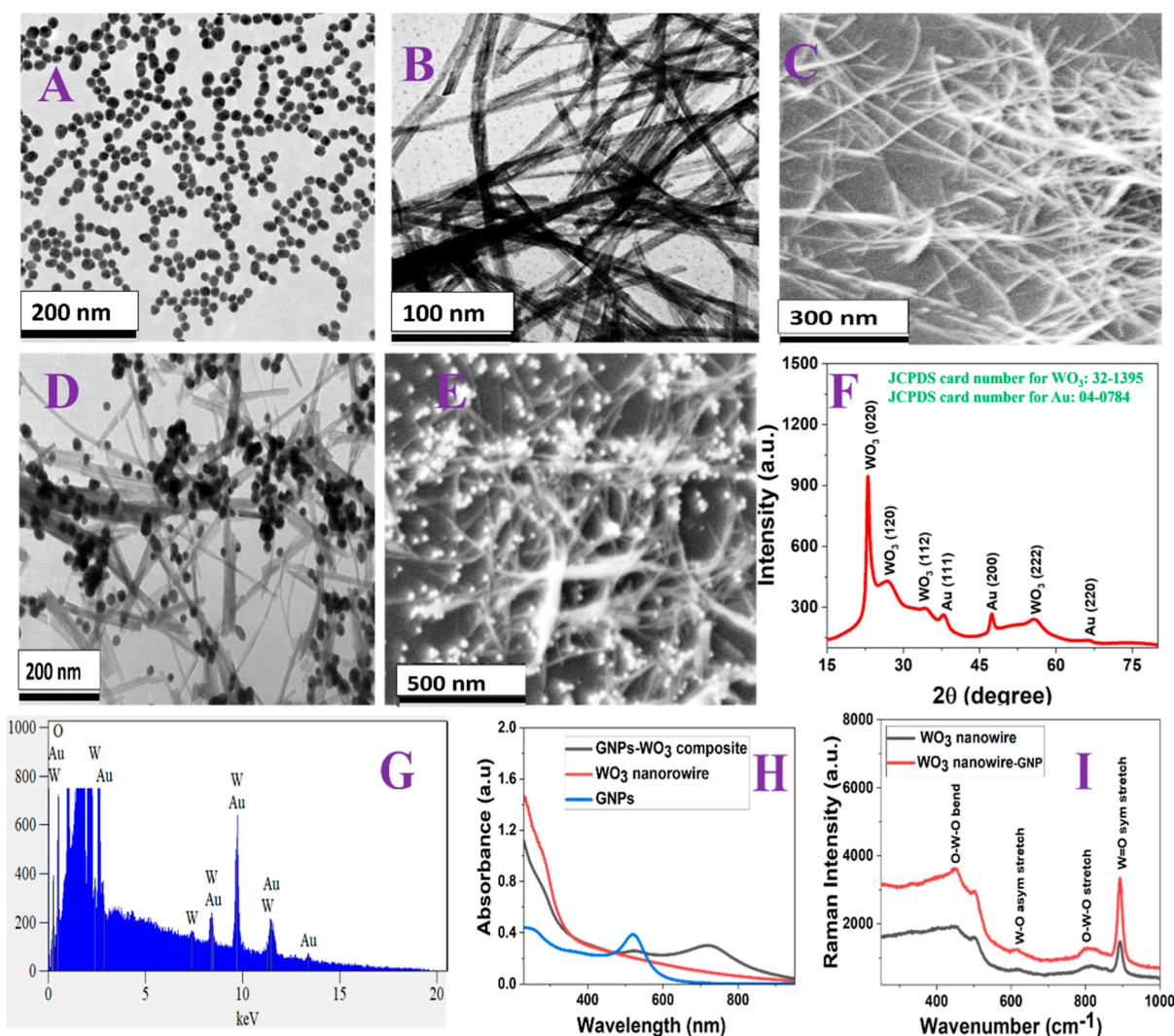
Figure 3. (A) TEM image of freshly prepared spherical GNPs with a diameter of 25 ± 2 nm. (B) TEM image of freshly prepared WO$_3$ nanowires. (C) SEM image of freshly prepared WO$_3$ nanowires. (D) TEM image of the freshly prepared GNP-decorated WO$_3$ nanowire-based heterojunction. (E) SEM image of the freshly prepared GNP-decorated WO$_3$ nanowire-based heterojunction. 2D r-GO-attached 1D WO$_3$ nanowire-based heterostructure. (F) XRD patterns from the heterojunction shows the Au (111), (200), and (220) planes for the GNP and (020), (120), (112), and (222) planes for WO$_3$. (G) EDX spectrum of the heterojunction shows the presence of Au, O, and W. (H) Absorption spectra of the spherical GNP, WO$_3$ nanowire, and heterojunction. (I) Raman spectra of the WO$_3$ nanowire and heterojunction show the presence of O−W−O stretching and bending, W−O symmetric stretching, and W−O asymmetric stretching bands from WO$_3$.

2. EXPERIMENTAL SECTION

2.1. Synthesis of Plasmonic GNPs.
We have synthesized plasmonic spherical shaped citrate-stabilized GNPs from H[AuCl$_4$]·3H$_2$O as a precursor according to our group's previous work,[49,50] as shown in Figure 2A. Experimental details are reported in the Supporting Information.

2.2. Synthesis of WO$_3$ Nanowires.
WO$_3$ nanowires were synthesized by the template/surfactant-free solvothermal synthetic approach using the methods reported by us and others,[24,35−43] as shown in Figure 2B. Experimental details are reported in the Supporting Information.

2.3. Development of the WO$_3$ Nanowire−Plasmonic GNP Heterojunction.
The plasmonic GNP- decorated WO$_3$ nanowire heterojunction was prepared with stirring by simply using a commercially available stirrer bar at room temperature. Experimental details are reported in the Supporting Information.

2.4. Finding the Photocatalytic Degradation of Methylene Blue Dye in the Presence of the Heterojunction and 670 nm Light.
To determine the photocatalytic degradation efficiency and degradation kinetics for methylene blue (MB) dye, we have exposed the dye−catalyst to 532 or 670 nm light for different time intervals. Experimental details are reported in the Supporting Information.

2.5. MRSA and CRE *E. coli* Pathogens Sample Preparation.
Different superbugs like MRSA and CRE *E. coli* were cultured according to the American type culture collection protocol, as we have reported before.[7,13,24−26,28,42] Experimental details are reported in the Supporting Information.

2.6. Finding the Possible Toxicity of the WO$_3$ Nanowire−Plasmonic GNP Heterojunction.
Possible toxicity of the GNP-decorated WO$_3$ nanowire-based heterojunction catalyst was determined using a cell viability test, as
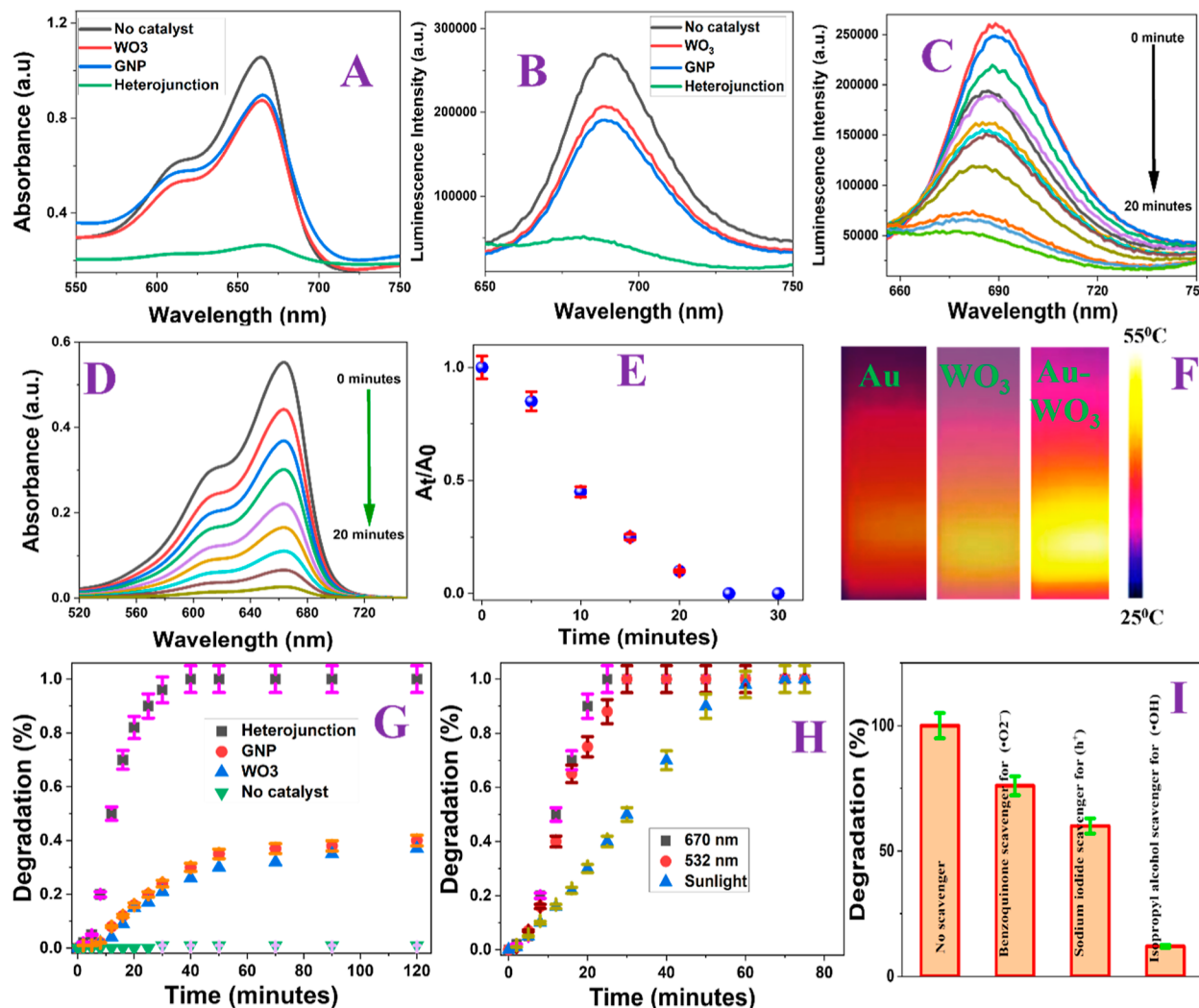
Figure 4. (A) Change of the absorption spectra of MB after exposure to 670 nm light for 20 min without the catalyst and with the WO$_3$ nanowire, GNP, and heterojunction catalyst. (B) Change of fluorescence spectra of MB after exposure to 670 nm light for 20 min without the catalyst and with the WO$_3$ nanowire, GNP, and heterojunction catalyst. (C) Time-dependent fluorescence intensity changes for MB during the exposure of 670 nm light in the presence of the heterojunction catalyst. (D) Time-dependent absorption intensity changes for MB during exposure to 670 nm light in the presence of the heterojunction catalyst. (E) Plot shows complete degradation of MB after exposure to 670 nm light for 25 min in the presence of the heterojunction catalyst. (F) Photograph shows IR thermography images of buffer in the presence of the WO$_3$ nanowire, GNP, and heterojunction catalyst when they are exposed to 670 nm NIR light for 15 min. (G) Degradation percentage changes with time for MB during the exposure to 670 nm light without the catalyst and with the WO$_3$ nanowire, GNP, and heterojunction catalyst. (H) Degradation percentage changes with time for MB during 670 and 532 nm light and sunlight exposure in the presence of the heterojunction catalyst. (I) Plot shows how the presence of different scavengers changes the degradation percentage of MB during 670 nm light exposure with the heterojunction catalyst.

we have reported before.[24,49,50] Experimental details are reported in the Supporting Information.

3. RESULTS AND DISCUSSION

3.1. Design and Characterization of the Plasmonic GNP-Decorated WO$_3$ Nanowire-Based Heterojunction. Spherical GNP-decorated WO$_3$ nanowire-based heterojunctions were designed using a three-step method, as shown in Figure 2. Initially, we synthesized plasmonic spherical shaped citrate-stabilized GNPs from H[AuCl$_4$]·3H$_2$O as a precursor according to our group's previous work,[42,49,50] as shown in Figure 2A. Experimental details are reported in the Supporting Information. The purified GNPs were kept at 4 °C for further use. At the end, GNPs were characterized using tunneling electron microscopy (TEM),[7,13,24−26,28,42,49,50] as reported in Figure 3A, which shows the spherical GNP with a diameter of

25 ± 2 nm. Figure 3H shows the absorption spectra of freshly prepared GNPs, which clearly show a strong plasmon band at 520 nm.

In the next step, WO$_3$ nanowires were synthesized by the template/surfactant-free solvothermal synthetic approach using our method and other reported methods,[24,37−41,45] as shown in Figure 2B. Synthesis details have been reported in the Supporting Information. At the end, the clear suspension was separated by centrifugation at 10,000 rpm for 5 min. Finally, the pure solid precipitate was washed repeatedly with distilled water and freeze-dried at −55 °C for a few days. At the end, the WO$_3$ nanowire was characterized using TEM and scanning electron microscopy (SEM),[7,13,24−26,28,42,49,50] as reported in Figure 3B,C, which indicates that the length is around 900 ± 300 nm and the diameter is around 20 ± 10 nm. Using energy-dispersive X-ray (EDX) data, as reported in Figure S1, and

atom % of elements contained, as reported in Table S1, we have determined the ratio of W and O to be 1:3. Figure 3I shows the Raman spectrum of freshly prepared nanowires, which indicates the presence of O−W−O stretching and bending, W−O symmetric stretching, and W−O asymmetric stretching bands from WO$_3$. Figure 3H shows the absorption spectra for WO$_3$ nanowires, which show strong absorption below 400 nm.

After that, the plasmonic GNPs-decorated WO$_3$ nanowire heterojunction was prepared with stirring by simply using a commercially available stirrer bar at room temperature, as shown in Figure 2. For this purpose, 25 mL of WO$_3$ nanowires (1 mg/mL) was added into a 100 mL round-bottom flask. Then, 25 mL of GNPs ($e = 265 \times 10^7$ mol^{-1} L cm^{-1}) was slowly injected under stirring, and stirring was continued vigorously for several hours. After that, the heterojunction was purified by centrifugation for 15 min at 5000 rpm. Finally, the solid was freeze-dried and kept in a refrigerator at 4 °C for future use. At the end, the plasmonic GNPs-decorated WO$_3$ nanowire heterojunction was characterized using TEM and SEM, as shown in Figure 3D,E, which clearly shows that GNPs are decorated on the WO$_3$ nanowire. Absorption spectra of the heterojunction, as reported in Figure 3H, clearly show a strong plasmon band at 520 nm, which indicates that GNPs are present in the heterojunction. As reported in Figure 3H, we have also observed a broad band between 640 and 750 nm, which is due to strong plasmon coupling between GNPs and the surface of the WO$_3$ nanowire. As shown in the TEM and SEM images reported in Figure 3D,E, GNPs are assembled on the WO$_3$ nanowire surface, and due to the plasmon coupling effect between the GNPs at the assembly, a new plasmon band is observed between 640 and 720 nm, which allows us to use NIR light for photocatalytic applications. EDX spectroscopy data[7,13,24−26,28,42,49,50] of the plasmonic GNP-decorated WO$_3$ nanowire heterojunction, reported in Figure 3G, show the presence of W, Au, and O. The X-ray powder diffraction (XRD) data[7,13,24−26,28,42,49,50] of freshly prepared WO$_3$ nanowires, as reported in Figure S2, show the (020), (120), (112), and (222) planes for WO$_3$ (JCPDS card number for WO$_3$: 32-1395).

Similarly, XRD data for freshly prepared plasmonic GNPs, as reported in Figure S2, show the (111), (200), (220), and (311) planes for Au (JCPDS card number for Au: 04-0784). Moreover, XRD data for the freshly prepared plasmonic GNPs-decorated WO$_3$ nanowire heterojunction, as reported in Figure 3F, show the presence of Au (111), (200), and (220) planes for GNPs (JCPDS card number for Au: 04-0784) and (020), (120), (112), and (222) planes for WO$_3$ (JCPDS card number for WO$_3$: 32-1395). Figure 3I shows the Raman spectra of the freshly prepared heterojunction, which indicate Raman intensity enhancement for the WO$_3$ bands such as O−W−O stretching and bending, W−O symmetric stretching, and W−O asymmetric stretching bands, which is due to the electromagnetic enhancement associated with the plasmon excitation of GNPs.[24,30,31,37−41,45]

3.2. Finding Photocatalytic Efficiency for the Plasmonic GNPs-Decorated WO$_3$ Nanowire Heterojunction at 670 nm Using MB Dye Degradation.

Next, to determine the photocatalytic activity for the plasmonic GNPs-decorated WO$_3$ nanowire heterojunction, we have used MB dye as a model dye.[24,30,31,37−41,45] As shown in Figure 3H, plasmonic GNPs-decorated WO$_3$ nanowire heterojunctions have strong absorption at 520 and 690 nm. As a result, for the

photocatalytic experiment, we used 532 nm visible light and 670 nm NIR light with 200 mW/cm^2 laser power. Although heterojunctions have strong absorption at 690 nm, we have used a 670 nm diode-pumped solid-state laser, which is a highly stable red laser available in our lab. To determine the photocatalytic degradation efficiency and degradation kinetics, we have used MB solution with an optical density of around ~1.0. For this purpose, we have added 2 mg/mL plasmonic GNPs-decorated WO$_3$ nanowire heterojunction catalyst or WO$_3$ catalyst or GNP catalyst. After that, the mixture of dye and the plasmonic GNPs-decorated WO$_3$ nanowire heterojunction catalyst was magnetically stirred for 1 h in the dark to reach the adsorption and desorption equilibrium. In the next step, the mixture was exposed to 532 or 670 nm light for different time intervals. To measure the photocatalytic degradation percentage, we measured the absorption and fluorescence of MB at different times during 670 nm light exposure, as shown in Figure 4A−D.
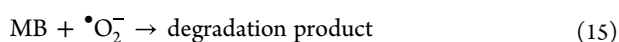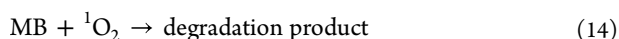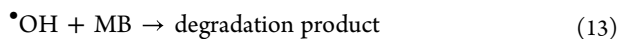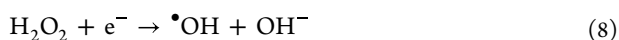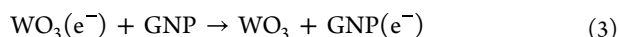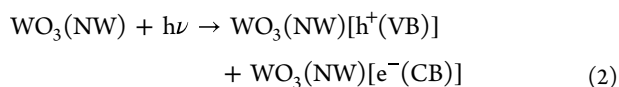
From the time-resolved absorption data, we have determined degradation efficiency using eq 1,[24,30,31,37−41,45]

$$
\text{degradation (\%)} = 100 \times \left[1 - \frac{A_t}{A_0} \right]_3 \tag{1}
$$

where A_0 is the absorption intensity at 665 nm from MB at time 0 and A_t is the absorption intensity at 665 nm from MB at time t. We performed the experiment five times to determine the error bar. Figure 4G shows how the time-dependent degradation percentage changes for MB during the exposure to 670 nm light in the absence of the catalyst, in the presence of the WO$_3$ nanowire catalyst, in the presence of the GNP catalyst, and in the presence of the GNP-decorated WO$_3$ nanowire-based heterojunction catalyst. Reported data indicate no degradation for MB in the absence of the catalyst, even after exposure to 670 nm light for 120 min. On the other hand, 20% degradation of MB has been observed after the exposure to 670 nm light for 120 min when the WO$_3$ nanowire catalyst has been used. Similarly, 15% degradation of MB has been observed after the exposure to 670 nm light for 120 min when the GNP catalyst has been used. Moreover, 100% degradation of MB has been observed after the exposure to 670 nm light for 25 min when the GNP-decorated WO$_3$ nanowire-based heterojunction catalyst has been used. The change of the absorption ratio (A_t/A_0) with time, as reported in Figure 4E, shows complete degradation of MB after exposure to 670 nm light for 25 min in the presence of the GNP-decorated WO$_3$ nanowire-based heterojunction catalyst. Reported experimental data clearly show that synergistic photocatalytic activity has been observed for the GNP-decorated WO$_3$ nanowire-based heterojunction in comparison to that with only the GNP or only the WO$_3$ nanowire catalyst.

3.3. Understanding the Photothermally Boosted Photocatalytic Degradation Mechanism.

The experimentally observed better photocatalytic activity for the GNP-decorated WO$_3$ nanowire-based heterojunction catalyst in comparison to that for the WO$_3$ nanowire-based catalyst or GNP catalyst can be attributed to several factors, which have been discussed below. In the case of the GNP-decorated WO$_3$ nanowire-based heterojunction photocatalyst, the localized SPR of the plasmonic GNP has the capability to enhance the light−matter interactions in the 670 nm region.[6,19,37−41,45] As reported in Figure 3H, the absorption spectra for the WO$_3$ nanowire show strong absorption below 400 nm and very low

absorption at 670 nm, which has been used for the photocatalytic reaction. On the other hand, as reported in Figure 3H, the GNP shows a strong plasmon band at 520 nm and very low absorption at 670 nm, which has been used for the photocatalytic reaction. As reported in Figure 3H, we have also observed a broad band between 640 and 750 nm, which is due to strong plasmon coupling between the GNPs and the surface of WO_3 nanowires.[6,19,37−41,45] Since GNPs are assembled on the WO_3 nanowire surface, the plasmon coupling effect between the GNPs at the assembly leads to a new plasmon band between 640 and 720 nm, and as a result, 670 nm has been used for the photocatalytic reaction. So, GNP assembly has been used to enhance the photocatalytic performance of the WO_3 nanowire via enhancing visible light absorption in the NIR region. As we have discussed before, the photocatalytic efficiency of the WO_3 nanowire is significantly low, which is mainly due to the high degree of the recombination process between holes (h^+) and electron (e^-) pairs.[25−40] Since the recombination process between e^- and h^+ restricts, WO_3 can be used in full capacity to produce ROS, which is the most important step for the photocatalytic process.[25−40] However, in the case of heterojunctions, due to the presence of GNPs, efficient separation of e^-/h^+ pairs occurs as shown in Figure 1, which helps generate more ROS, which enhances the degradation. Equations 2−15 show the possible degradation mechanism for MB using the GNP-decorated WO_3 nanowire-based heterojunction-based photocatalyst.[21−35,41]

$$WO_3(NW) + h\nu \rightarrow WO_3(NW)[h^+(VB)]$$
$$+ WO_3(NW)[e^-(CB)] \tag{2}$$

$$WO_3(e^-) + GNP \rightarrow WO_3 + GNP(e^-) \tag{3}$$

$$GNP(e^-) + O_2 \rightarrow {}^\bullet O_2^- + GNP \tag{4}$$

$${}^\bullet O_2^- + H^+ \rightarrow {}^\bullet HO_2 \tag{5}$$

$${}^\bullet HO_2 + e^- \rightarrow HO_2^- \tag{6}$$

$$HO_2^- + H^+ \rightarrow H_2O_2 \tag{7}$$

$$H_2O_2 + e^- \rightarrow {}^\bullet OH + OH^- \tag{8}$$

$${}^\bullet O_2^- + h^+ \rightarrow {}^1O_2 \tag{9}$$

$$h^+ + H_2O \rightarrow {}^\bullet OH + H^+ \tag{10}$$

$$h^+ + OH^- \rightarrow {}^\bullet OH \tag{11}$$

$${}^\bullet OH + {}^\bullet OH \rightarrow H_2O_2 \tag{12}$$

$${}^\bullet OH + MB \rightarrow \text{degradation product} \tag{13}$$

$$MB + {}^1O_2 \rightarrow \text{degradation product} \tag{14}$$

$$MB + {}^\bullet O_2^- \rightarrow \text{degradation product} \tag{15}$$

As reported in eqs 2−15, due to the strong oxidizing abilities of holes, the h^+ helps form the hydroxy radicals (${}^\bullet OH$) by oxidizing water.[21−35,41] The hydroxy radicals (${}^\bullet OH$) formed by the above reaction can combine with each other to form hydrogen peroxide.[21−35,41] On the other hand, due to the strong reducing abilities of electrons, e^- helps form the superoxide radical (${}^\bullet O_2^-$) by reducing the oxygen mole-

cule.[21−35,41] In the next step, some superoxide radicals (${}^\bullet O_2^-$) combine with holes and form singlet oxygen (${}^1O_2$).[21−35,41] All ROS formed by electron and holes [(${}^\bullet OH$), (${}^\bullet O_2^-$), and (${}^1O_2$)] are highly active oxidants that have capabilities to degrade MB.[21−35,41] It is now well documented that due to the localized plasmon surface resonance, GNPs can absorb light and act as photothermal agents. During this process, GNPs have the capability to convert light energy into heat via nonradiation processes. As we and others have discussed before, when light interacts with metal nanoparticles, depending on the excitation cross-section, the amount of photons absorbed by plasmonic nanoparticles will be released either via emission of photons, which is known as luminescence, or as generated heat via the formation of phonons.[6,7,19,24,49−51]

Since the luminescence quantum yield for plasmonic nanoparticles is below 1%, one can assume that most of the absorbed energy will be transformed into heat.[6,7,19,24,49−51] As reported in Figure 3H, since the light absorption cross-section for the assembly of GNPs on the GNP-decorated WO_3 nanowire-based heterojunction catalyst is very high at 670 nm, it will exhibit strong light-to-heat conversion ability at 670 nm excitation.

The photograph in Figure 4F shows IR thermography images of buffer in the presence of the WO_3 nanowire, GNP, and heterojunction catalyst when they are exposed to 670 nm NIR light for 15 min. The IR thermography images indicate that the maximum temperature increases to 52 °C in the case of the heterojunction catalyst. On the other hand, the temperature increased to only 41 °C in the presence of the WO_3 nanowire, which is also due to the very low absorption capacity of the WO_3 nanowire at 670 nm. Similarly, the temperature increased to about 36 °C when the GNP nanoparticle was exposed to 670 nm light, and it is due to the very low absorption capacity for GNPs at 670 nm. The photothermal conversion efficiencies (η) for the WO_3 nanowire, GNP nanoparticle, and heterostructure were calculated using eq S1 reported in the Supporting Information, which indicates that the photothermal efficiency for the heterojunction catalyst (37.3%) is much higher than that of the WO_3 nanowire (21.4%) and GNP (15.8%). All the above photothermal experiments indicate that during 670 nm light exposure, due to the photothermal effect, the temperature increase is around 24 °C in the presence of the GNP-decorated WO_3 nanowire-based heterojunction photocatalyst. As a result, the photogenerated electrons could gain heat energy and move faster, which improves the charge separation efficiency and enhances the ROS formation amount to increase the degradation efficiency.[6,7,19,35−45] Similarly, the photothermal effect of the GNP can enhance the local temperature of the WO_3 photocatalyst surface, which can reduce the activation energy of the reaction and improve the charge separation efficiency.[6,7,19,24,35−45]

Next, we have used different scavengers to determine whether hydroxyl radicals (${}^\bullet OH$), superoxide radicals (${}^\bullet O_2^-$), and holes (h^+) are the necessary ROS for the photocatalytic decomposition of MB.[6,7,19,24,35−45] In this case, we have used benzoquinone as a scavenger for superoxide radicals (${}^\bullet O_2^-$), which is a well-known trapping agent/scavenger for superoxide radicals.[6,7,19,24,35−45] On the other hand, we have used isopropyl alcohol (IPA) as a scavenger for hydroxyl radicals (${}^\bullet OH$), which is well-known trapping agent/scavengers for hydroxyl radicals.[6,7,19,24,35−45] Similarly, we have used a sodium iodide scavenger for holes (h^+), which is a well-known trapping
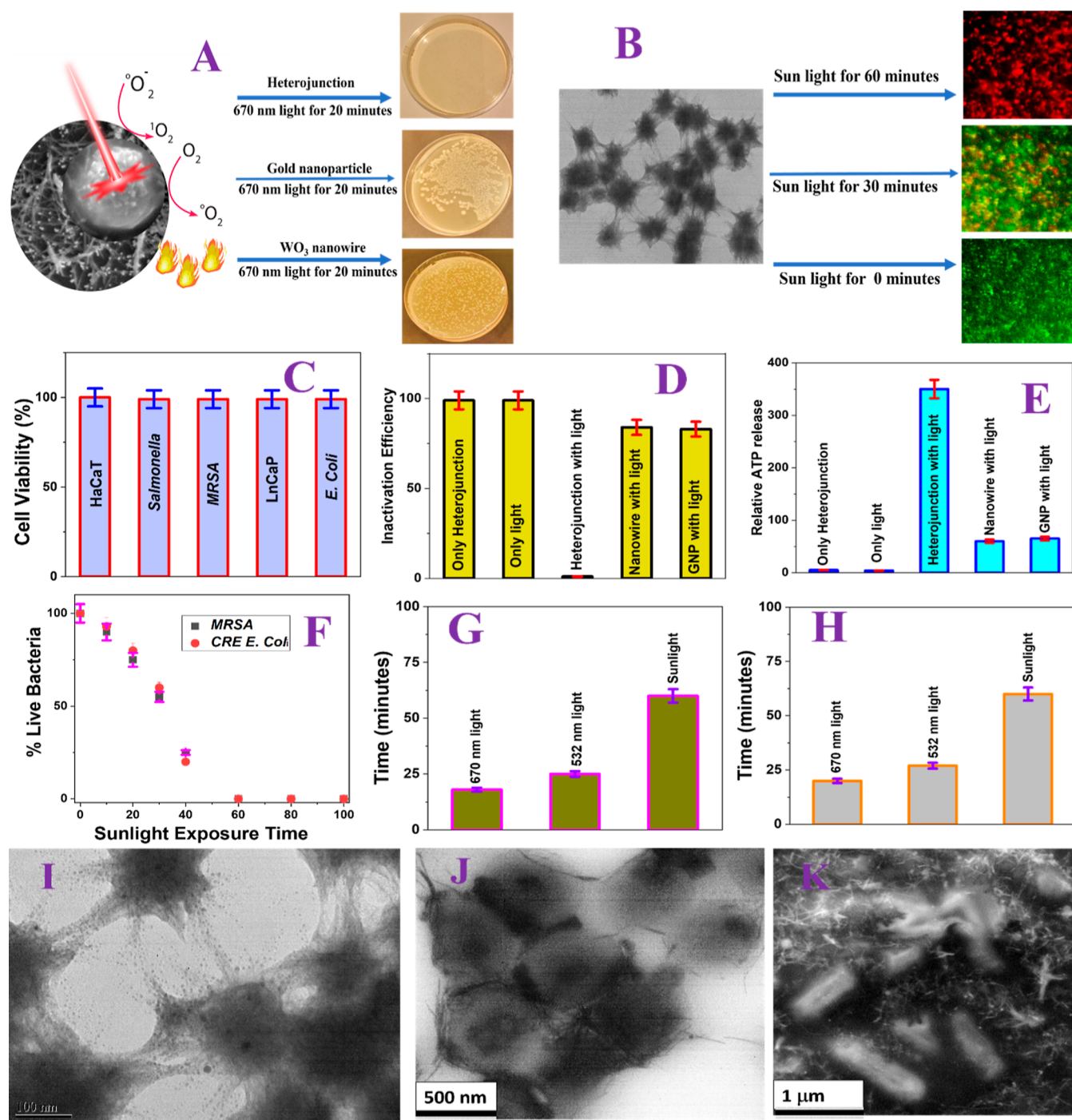
Figure 5. (A) MRSA inactivation efficiency after exposure to 670 nm light for 20 min in the presence of the WO_3 nanowire, GNP, and heterojunction catalyst. (B) MRSA inactivation efficiency in the presence of sunlight at different time intervals when the heterojunction catalyst is present. (C) Biocompatibility of the heterojunction catalyst against different cells in the absence of light. (D) MRSA inactivation efficiency in the presence of the heterojunction catalyst without light, only light, light with the heterojunction catalyst, GNPs catalyst, and WO_3 nanowire catalyst. (E) Relative cellular ATP leakage percentage from MRSA in the presence of the heterojunction catalyst without light, with light only, and with light in the presence of the heterojunction catalyst, GNPs catalyst, and WO_3 nanowire catalyst. (F) Plot shows time-dependent superbug inactivation efficiency in the presence of sunlight and the heterojunction catalyst. (G) Plot shows time required for 100% MRSA inactivation in the presence of 670 and 532 nm light and sunlight using the heterojunction catalyst. (H) Plot shows time required for 100% of CRE *E. coli* inactivation in the presence of 670 and 532 nm light and sunlight using the GNPs-decorated WO_3 nanowire heterojunction catalyst. (I) TEM image shows that heterojunction wraps the MRSA bacterial surface. (J) SEM image shows high membrane damage on the superbug surface when MRSA bacteria are exposed to sunlight and heterojunction catalysts for 60 min. (K) SEM image shows high membrane damage on the superbug surface when CRE *E. coli* bacteria are exposed to sunlight and heterojunction catalysts for 60 min.

agent/scavenger for hydroxyl radicals.[6,7,19,24,35−45] Figure 4I shows how the presence of different scavengers change the

degradation percentage of MB during 670 nm light exposure in the presence of the GNP-decorated WO_3 nanowire-based

heterojunction. From the reported experimented data, one can clearly see that IPA is the most effective scavenger.[6,7,19,24,35−45] Similarly, the scavenger efficiency for sodium iodide is higher than that for benzoquinone. Reported experimental data clearly show that hydroxyl radicals ($^\bullet$OH), superoxide radicals ($^\bullet$O$_2^-$), and holes (h$^+$) are the necessary ROS for the photocatalytic decomposition of MB using the GNP-decorated WO$_3$ nanowire-based heterojunction photocatalyst.

3.4. Understanding Wavelength-Dependent Photocatalytic Efficiency for the Plasmonic GNPs-Decorated WO$_3$ Nanowire Heterojunction.

Next, we have determined a wavelength-dependent photocatalytic degradation experiment of MB using a GNP-decorated WO$_3$ nanowire-based heterojunction photocatalyst. In this case, we have used 532 and 670 nm light from green and red lasers. As shown in Figure 3H, the plasmonic GNPs-decorated WO$_3$ nanowire heterojunction has strong absorption at 520 and 690 nm. As a result, for the photocatalytic experiment, we used 532 nm visible light and 670 nm NIR light with 200 mW/cm^2 laser power. As shown in Figure 4H, 100% degradation of MB has been observed after the exposure to 670 nm light for 25 min when the GNP-decorated WO$_3$ nanowire-based heterojunction catalyst has been used. On the other hand, as shown in Figure 4H, 100% degradation of MB has been observed after the exposure to 532 nm light for 35 min when the GNP-decorated WO$_3$ nanowire-based heterojunction catalyst has been used. The above data clearly show that the degradation kinetics is superior at 670 nm excitation than at 532 nm excitation. As reported in Figure 3H, the plasmon coupling effect between the GNPs at the assembly leads to a new plasmon band between 640 and 720 nm. As a result, during 670 nm excitation, GNP assembly has been used to enhance the photocatalytic performance of WO$_3$ nanorods via enhancing visible light absorption in the NIR region. Since it is well documented that catalytic reactions mainly happen on the surface of nanoparticles,[6,7,19,24,35−45] an increase in the accessible surface area via self-assembly would considerably improve the catalyst's efficiency. We have also measured the photothermal conversion efficiency (η) for the heterostructure, which was calculated using eq S1 reported in the Supporting Information, which indicates the photothermal efficiency for the heterojunction catalyst (37.3%) when excited at 670 nm light. On the other hand, the photothermal efficiency for the heterojunction catalyst is 30.8% when excited at 532 nm light, which is due to lower absorption efficiency at 532 nm than at 670 nm excitation for the heterojunction catalyst. Due to the lower temperature increase, the photothermally boosted photocatalytic degradation rate is lower.

3.5. Determining Sunlight-Based Photocatalytic Efficiency for the Plasmonic GNPs-Decorated WO$_3$ Nanowire Heterojunction.

As we have discussed before, sunlight is a renewable energy source that is the most efficient and easily available[6,7,19,24,35−45] source, so to determine the possible practical application, we have also performed the same experiment under sunlight illumination. For this purpose, we have used a full spectrum natural sunlight 200 W light bulb. As reported in Figure 4H, the sunlight illumination degrades 100% of MB after 60 min exposure in the presence of the GNP-decorated WO$_3$ nanowire-based heterojunction catalyst (6 mg/mL). We have also performed the same experiment using natural sunlight, and experimental data indicate that the natural sunlight illumination degrades 100% of MB after 60 min of exposure of sunlight in the presence of the GNP-

decorated WO$_3$ nanowire-based heterojunction catalyst (6 mg/mL). The observed lower degradation rate in the presence of natural sunlight is due to the low power of light. Since laser light is focused, the power density is much higher for laser light than that for sunlight. As we have discussed before, for the photocatalytic experiment, we used 532 nm visible light and 670 nm NIR light with 200 mW/cm^2 laser power. On the other hand, the power density of the sunlight was approximately 44 mW/cm^2. Since laser light is focused, the power density is much higher for laser light; as a result, we have observed higher degradation for laser light. We also measured the temperature, which indicates that the temperature enhancement is very low, and as a result, the photothermal contribution will be lower for sunlight excitation.

3.6. Finding the Biocompatibility of the GNP-Decorated WO$_3$ Nanowire-Based Heterojunction.

For real life application of the photothermally boosted photocatalytic material in society, biocompatibility of the GNP-decorated WO$_3$ nanowire-based heterojunction catalyst in the absence of light is the most important parameter.[6,7,19,24,35−45] For determining the biocompatibility, we have performed cytotoxicity experiments using different normal and cancer cell lines such as HaCaT normal skin cells and LnCaP prostate cancer cells. In this case, we have used 4.6×10^5 cells/mL LnCaP prostate cancer cells and 4.2×10^5 cells/mL HaCaT normal cells.[24,28,49,50] Similarly, we have also performed biocompatible experiments against MRSA, *Salmonella,* and CRE *E. coli.*[24,28,49,50] In this case, we have used 1.6×10^5 cfu/mL *Salmonella,* 2.2×10^5 cfu/mL MRSA, and 1.2×10^5 cfu/mL CRE *E. coli* LnCaP and HaCaT cell lines, and all bacteria were incubated with the GNP-decorated WO$_3$ nanowire-based heterojunction catalyst for 24 h. After that, the cell viability for SK-BR-3 breast cancer cells and HaCaT normal cells was measured using the MTT colorimetric test.[24,26−28,49,50] Similarly, we have used the colony counting technique and LIVE/DEAD *Bac*Light Bacterial Viability Kits to determine the number of live bacteria after the photocatalytic process.[7,13,24,26−28,49,50] As reported in Figure 5C, the biocompatibility data of the plasmonic GNPs-decorated WO$_3$ nanowire heterojunction against HaCaT normal skin cells, LnCaP prostate cancer cells, MRSA, *Salmonella,* and CRE *E. coli* in the absence of light show about 99% cell viability even after 24 h of incubation. The above data clearly indicate that the GNPs-decorated WO$_3$ nanowire heterojunction is not cytotoxic in the absence of light.

3.7. Finding the 670 nm Based Superbug Inactivation Efficiency Using the Plasmonic GNPs-Decorated WO$_3$ Nanowire Heterojunction via a Photothermally Boosted Photocatalytic Mechanism.

Next, to determine the 670 nm-based superbug inactivation efficiency using the plasmonic GNPs-decorated WO$_3$ nanowire heterojunction via a photothermally boosted photocatalytic mechanism, we have performed a 670 nm light and sunlight-based exposure experiment. In this case, for the photocatalytic inactivation experiment, we have used MRSA and CRE *E. coli.*[7,13,24,26−28] Experimental details have been reported in the Supporting Information. The superbug inactivation test has been performed using the GNP-decorated WO$_3$ nanowire-based heterojunction catalyst, WO$_3$ nanowire catalyst, and GNP catalyst, as reported in Figure 5A. After the exposure of superbugs to 670 nm or sunlight in the presence of different catalysts for different time intervals, the superbug inactivation efficiency was determined using the colony counting

technique,[7,13,24,26−28] as reported in Figure 5A. Similarly, we have also used LIVE/DEAD BacLight Bacterial Viability Kits[7,13,24,26−28] to find the inactivation efficiency in the presence of different catalysts, as reported in Figure 5B, where SYTO 9 green-fluorescent stain has been used for the imaging of live bacteria and propidium iodide red-fluorescent stain for the imaging of dead bacteria via a binding event.[7,13,24,26−28]

As reported in Figure 5A, we have observed 100% inactivation of MRSA superbugs after exposure to 670 nm light for 20 min in the presence of the GNP-decorated WO₃ nanowire-based heterojunction catalyst. The observed 100% inactivation efficiency is due to the multimodal photocatalytic and photothermal inactivation of superbugs when we have used a GNP-decorated WO₃ nanowire-based heterojunction catalyst. On the other hand, we observed 20% inactivation of MRSA superbugs after exposure to 670 nm light for 20 min in the presence of the WO₃ nanowire-based catalyst. The observed 20% inactivation efficiency is due to the occurrence of only photocatalytic inactivation of superbugs when we have used the WO₃ nanowire-based catalyst. Similarly, we have observed 25% inactivation of MRSA superbugs after exposure to 670 nm light for 20 min in the presence of the GNP catalyst. The observed 25% inactivation efficiency is due to the occurrence of only photothermal inactivation of superbugs when we have used a GNP-based catalyst.

3.8. Understanding the Photothermally Boosted Photocatalytic Inactivation Mechanism.

As we have discussed, 100% inactivation efficiency in the presence of the GNP-decorated WO₃ nanowire-based heterojunction catalyst is due to the photothermally enhanced photocatalytic inactivation mechanism. As reported in Figure 3H, due to high absorption at 670 nm for the assembly of GNPs on the GNP decorated WO₃ nanowire-based heterojunction catalyst, it has strong light-to-heat conversion ability during exposure to 670 nm light. Figure 4F shows that the temperature increased to about 49 °C when the GNP-decorated WO₃ nanowire-based heterojunction photocatalyst was exposed to 670 nm light. As we have discussed before, since the temperature increase is around 24 °C in the presence of the GNP-decorated WO₃ nanowire-based heterojunction photocatalyst, the photogenerated electrons could gain the heat energy and move faster, which improves the charge separation efficiency and enhances the ROS formation amount to increase the inactivation efficiency.[35−45] Similarly, the photothermal effect of the GNP can enhance the local temperature of the WO₃ photocatalyst surface, which can reduce the activation energy of the reaction and improve the charge separation efficiency.[45−51]

The reported SEM image in Figure 5I indicates that the GNP-decorated WO₃ nanowire-based heterojunction catalyst wraps the MRSA superbugs and generates significant membrane stress for MRSA. As reported in Figure 5J, when MRSA superbugs are exposed to light in the presence of the GNP-decorated WO₃ nanowire-based heterojunction catalyst, significant membrane damage results on the surface of MRSA superbugs. Similarly, the SEM image reported in Figure 5K indicates that when CRE E. coli superbugs are exposed to light in the presence of the GNP-decorated WO₃ nanowire-based heterojunction catalyst, significant membrane damage results on the surface of CRE E. coli superbugs. This pore formation due to membrane damage for MRSA and CRE E. coli superbugs allows higher diffusion of ROS such as holes,

hydroxyl radicals, and superoxide radicals inside superbugs, which increases the rate of collapse of superbugs via transmembrane leakage of adenosine triphosphate (ATP), deoxyribonucleic acid (DNA)/ribonucleic acid (RNA), etc.[7,13,24,26−28] Since ATP is an important indicator of cell viability, to better understand the above-discussed mechanism, we have measured the superbug ATP leakage amount after light exposure for MRSA and CRE E. coli superbugs using the ATP kit.[7,13,24,26−28] ATP leakage data during light exposure as reported in Figure 5E show maximum leakage of cellular ATP when superbugs are exposed to light in the presence of the GNP-decorated WO₃ nanowire-based heterojunction catalyst.

3.9. Finding Wavelength-Dependent Superbugs Inactivation Efficiency for the Plasmonic GNPs-Decorated WO₃ Nanowire Heterojunction Catalyst.

Next, we have determined the wavelength-dependent superbug inactivation efficiency using a GNP-decorated WO₃ nanowire-based heterojunction photocatalyst. For this purpose, we have used 532 and 670 nm light from green and red lasers. As shown in Figure 5G,H, plasmonic GNPs-decorated WO₃ nanowire heterojunctions have strong absorption at 520 and 690 nm. As a result, for the photocatalytic experiment, we used 532 nm visible light and 670 nm NIR light with 200 mW/cm² laser power. As shown in Figure 5G, 100% inactivation of MRSA superbugs has been observed after the exposure to 670 nm light for 20 min when the GNP-decorated WO₃ nanowire-based heterojunction catalyst has been used. On the other hand, as shown in Figure 5G, 100% inactivation of MRSA superbugs has been observed after the exposure to 532 nm light for 26 min when the GNP-decorated WO₃ nanowire-based heterojunction catalyst has been used. Similarly, as shown in Figure 5H, 100% inactivation of the CRE E. coli superbug has been observed after the exposure to 670 nm light for 18 min when the GNP-decorated WO₃ nanowire-based heterojunction catalyst has been used. On the other hand, as shown in Figure 5H, 100% inactivation of MRSA superbugs has been observed after the exposure to 532 nm light for 26 min when the GNP-decorated WO₃ nanowire-based heterojunction catalyst has been used. The above data clearly show that the superbug inactivation kinetics is superior at 670 nm excitation compared to that for 532 nm excitation. As reported in Figure 3H, due the plasmon coupling effect between the GNPs at the assembly, a new plasmon band is observed between 640 and 720 nm, and as a result, during 670 nm excitation, GNP assembly has been used to enhance the photocatalytic performance of the WO₃ nanorod via enhancing visible light absorption in the NIR region. Since it is well documented that catalytic reactions mainly happen on the surface of nanoparticles, an increase in the accessible surface area via self-assembly would considerably improve the catalyst's efficiency. As we have discussed before, the temperature increase is around 24 °C when 670 nm excitation has been used, and the temperature increase is around 19 °C when 532 nm excitation has been used. Due to the lower temperature increase, the photothermally boosted photocatalytic inactivation of superbugs rate is lower for 532 nm excitation.

3.10. Determining Sunlight-Based Superbugs in Activation Efficiency Using the Plasmonic GNPs-Decorated WO₃ Nanowire Heterojunction.

As we have discussed before, sunlight is a renewable energy source that is the most efficient and easily available source. Next, to determine the possible practical application, we also performed

the same experiment under sunlight illumination. For this purpose, we have used a full spectrum natural sunlight 200 W light bulb (42 mW/cm^2). As reported in Figure 5B, sunlight illumination can kill 100% MRSA after 60 min of exposure to sunlight in the presence of the GNP-decorated WO$_3$ nanowire-based heterojunction catalyst (6 mg/mL). The observed red fluorescence after 60 min sunlight exposure as shown in Figure 5B is due to the dead MRSA, which binds with propidium iodide red-fluorescent nucleic acid stain. Similarly, the observed green fluorescence after zero minute sunlight exposure, as shown in Figure 5B, is due to the live MRSA, which binds with SYTO 9 green, fluorescent stain.[7,13,24,26−28] Reported MRSA viability data in Figure 5B also show yellow fluorescence after 30 min sunlight exposure, which is due to the overlap between green color from live MRSA and red color from dead MRSA. Figure 5F−H shows time-dependent superbug inactivation efficiency for CRE *E. coli* and MRSA in the presence of sunlight and the GNPs-decorated WO$_3$ nanowire heterojunction catalyst, which indicates that in both cases, 60 min of exposure to sunlight is necessary for 100% inactivation of superbugs. We have also performed the same experiment using natural sunlight, and experimental data indicate that the natural sunlight illumination degrades 100% MB after 140 min of exposure in the presence of the GNP-decorated WO$_3$ nanowire-based heterojunction catalyst (6 mg/mL). The observed lower inactivation rate in the presence of natural sunlight is due to the low power of light. We have also measured the temperature, which indicates that the temperature enhancement is very low, and as a result, the photothermal contribution will be lower.

4. CONCLUSIONS

Herein, our findings reveal that the GNP-decorated WO$_3$ nanowire-based heterojunction catalyst has the capability for 100% combating of superbugs under sunlight. Moreover, 670 nm NIR light-based photocatalytic activity demonstrated 100% degradation of MB dye in the presence of the heterojunction catalyst, which is much higher than that with only the WO$_3$ nanowire (20%) or GNP (15%). The observed higher photocatalytic performance for the heterojunction is due to the enhanced absorption capability of the plasmonic GNP at 670 nm and increase in temperature of the photocatalyst surface via the photothermal effect, which reduces the activation energy of the degradation reaction. Our experimental finding shows that the temperature increase is around 24 °C in the presence of the GNP-decorated WO$_3$ nanowire-based heterojunction photocatalyst. As a result, the photogenerated electrons move faster, which improves the charge separation efficiency and enhances the ROS formation amount to increase the degradation efficiency. Photocatalytic experimental data with different scavengers reveal that hydroxyl radicals ($^\bullet$OH) play an important role in the photocatalytic degradation of MB using a GNP-decorated WO$_3$ nanowire-based heterojunction catalyst.

Our investigation shows that the photothermally boosted photocatalytic performance is much superior to that of only the photocatalytic or photothermal process. Sunlight-driven photocatalytic experiments show 100% inactivation of CRE *E. coli* and MRSA after 60 min of light irradiation. Reported SEM image shows that when superbugs are exposed to light in the presence of the GNP-decorated WO$_3$ nanowire-based heterojunction catalyst, it results in significant membrane damage on the surface of superbugs, which allows higher diffusion of ROS inside superbugs. The above process increases the rate of collapse of superbugs via transmembrane leakage of ATP and DNA/RNA. We envision that sunlight-driven inactivation of superbugs using a photothermal−photocatalytic heterojunction is a powerful approach for combating drug-resistant bacteria.

■ ASSOCIATED CONTENT

Ⓢ Supporting Information

The Supporting Information is available free of charge at https://pubs.acs.org/doi/10.1021/acsomega.4c05327.

> Design and characterization of the GNP-decorated WO$_3$ nanowire-based heterojunction catalyst and other experiments such as MB degradation and superbug inactivation (PDF)

■ AUTHOR INFORMATION

Corresponding Author

Paresh Chandra Ray − *Department of Chemistry and Biochemistry, Jackson State University, Jackson, Mississippi 39217, United States;* ⊙ orcid.org/0000-0001-5398-9930; Email: paresh.c.ray@jsums.edu; Fax: +16019793674

Authors

Avijit Pramanik − *Department of Chemistry and Biochemistry, Jackson State University, Jackson, Mississippi 39217, United States;* ⊙ orcid.org/0000-0002-4623-2099

Shivangee Rai − *Department of Chemistry and Biochemistry, Jackson State University, Jackson, Mississippi 39217, United States*

Kaelin Gates − *Department of Chemistry and Biochemistry, Jackson State University, Jackson, Mississippi 39217, United States*

Olorunsola Praise Kolawole − *Department of Chemistry and Biochemistry, Jackson State University, Jackson, Mississippi 39217, United States*

Sanchita Kundu − *Department of Chemistry and Biochemistry, Jackson State University, Jackson, Mississippi 39217, United States;* ⊙ orcid.org/0000-0002-9843-0476

Pragathi Kasani-Akula − *Department of Chemistry and Biochemistry, Jackson State University, Jackson, Mississippi 39217, United States*

Jagriti Singh − *Department of Chemistry and Biochemistry, Jackson State University, Jackson, Mississippi 39217, United States*

Jerusha Dasary − *Department of Chemistry and Biochemistry, Jackson State University, Jackson, Mississippi 39217, United States*

Huimin Zhang − *Department of Chemistry and Biochemistry, Jackson State University, Jackson, Mississippi 39217, United States;* ⊙ orcid.org/0000-0002-0218-1410

Fengxiang X. Han − *Department of Chemistry and Biochemistry, Jackson State University, Jackson, Mississippi 39217, United States;* ⊙ orcid.org/0000-0001-5135-3031

Complete contact information is available at:
https://pubs.acs.org/10.1021/acsomega.4c05327

Notes

The authors declare no competing financial interest.

■ REFERENCES

(1) WHO. Antimicrobial Resistant Fact Sheet. http://www.who.int/mediacentre/factsheets/fs194/en/ (accessed Dec 8, 2022).

(2) Theuretzbacher, U.; Bush, K.; Harbarth, S.; Paul, M.; Rex, J. H.; Tacconelli, E.; Thwaites, G. E. Critical analysis of antibacterial agents in clinical development. *Nat. Rev. Microbiol.* **2020**, *18*, 286−298.

(3) Gao, W.; Zhang, L. Nanomaterials Arising Amid Antibiotic Resistance. *Nat. Rev. Microbiol.* **2021**, *19*, 5−6.

(4) Doolan, J. A.; Williams, G. T.; Hilton, K. L. F.; Chaudhari, R.; Fossey, J. S.; Goult, B. T.; Hiscock, J. R. Advancements in antimicrobial nanoscale materials and self-assembling systems. *Chem. Soc. Rev.* **2022**, *51*, 8696−8755.

(5) Roope, L. S. J.; Smith, R. D.; Pouwels, K. B.; Buchanan, J.; Abel, L.; Eibich, P.; Butler, C. C.; Tan, P. S.; Walker, A. S.; Robotham, J. V.; Wordsworth, S. The Challenge of Antimicrobial Resistance: What Economics Can Contribute. *Science* **2019**, *364*, 41−49.

(6) Ran, B.; Ran, L.; Wang, Z.; Liao, J.; Li, D.; Chen, K.; Cai, W.; Hou, J.; Peng, X. Photocatalytic Antimicrobials: Principles, Design Strategies, and Applications. *Chem. Rev.* **2023**, *123*, 12371−12430.

(7) Begum, S.; Pramanik, A.; Davis, D.; Patibandla, S.; Gates, K.; Begum, S.; Ray, P. C. 2D and Heterostructure Nanomaterial Based Strategies for Combating Drug-Resistant Bacteria. *ACS Omega* **2020**, *5*, 3116−3130.

(8) Gupta, A.; Mumtaz, S.; Li, C.-H.; Hussain, I.; Rotello, V. M. Combatting antibiotic-resistant bacteria using nanomaterials. *Chem. Soc. Rev.* **2019**, *48*, 415−427.

(9) Richards, T.; Harrhy, J. H.; Lewis, R. J.; Howe, A. G. R.; Suldecki, G. M.; Folli, A.; Morgan, D. J.; Davies, T. E.; Loveridge, E. J.; Crole, D. A.; Edwards, J. K.; Gaskin, P.; Kiely, C. J.; He, Q.; Murphy, D. M.; Maillard, J.-Y.; Freakley, S. J.; Hutchings, G. J. A residue-free approach to water disinfection using catalytic in situ generation of reactive oxygen species. *Nat. Catal.* **2021**, *4*, 575−585.

(10) Qi, X.; Huang, Y.; You, S.; Xiang, Y.; Cai, E.; Mao, R.; Pan, W.; Tong, X.; Dong, W.; Ye, F.; Shen, J. Engineering Robust Ag-Decorated Polydopamine Nano-Photothermal Platforms to Combat Bacterial Infection and Prompt Wound Healing. *Adv. Sci.* **2022**, *9*, 2106015.

(11) Wang, S.; Qiao, Y.; Liu, X.; Zhu, S.; Zheng, Y.; Jiang, H.; Zhang, Y.; Shen, J.; Li, Z.; Liang, Y.; Cui, Z.; Chu, P. K.; Wu, S. Reduced Graphene Oxides Modified Bi2Te3 Nanosheets for Rapid Photo-Thermoelectric Catalytic Therapy of Bacteria-Infected Wounds. *Adv. Funct. Mater.* **2023**, *33*, 2210098.

(12) Dik, D. A.; Fisher, J. F.; Mobashery, S. Cell-Wall Recycling of the Gram-Negative Bacteria and the Nexus to Antibiotic Resistance. *Chem. Rev.* **2018**, *118*, 5952−5984.

(13) Ray, P. C.; Khan, S. A.; Singh, A. K.; Senapati, D.; Fan, Z. Nanomaterials for Targeted Detection and Photothermal Killing of Bacteria. *Chem. Soc. Rev.* **2012**, *41*, 3193−3209.

(14) Sun, J.; Chen, X.; Mo, S.; Zhang, Z.; Guo, D.; Li, Y.; Liu, L. Recent Advances of Bismuth Halide Based Nanomaterials for Photocatalytic Antibacterial and Photodynamic Therapy. *Adv. Mater. Interfaces.* **2022**, *9*, 2200704.

(15) Wei, Z.; Wang, W.; Li, W.; Bai, X.; Zhao, J.; Tse, E. C. M.; Phillips, D. L.; Zhu, Y. Steering Electron-Hole Migration Pathways Using Oxygen Vacancies in Tungsten Oxides to Enhance Their Photocatalytic Oxygen Evolution Performance. *Angew. Chem., Int. Ed.* **2021**, *60* (15), 8236−8242.

(16) Wang, W.; Song, Q.; Luo, Q.; Li, L.; Huo, X.; Chen, S.; Li, J.; Li, Y.; Shi, S.; Yuan, Y.; Du, X.; Zhang, K.; Wang, N. Photothermal-enabled single-atom catalysts for high-efficiency hydrogen peroxide photosynthesis from natural seawater. *Nat. Commun.* **2023**, *14* (1), 2493.

(17) Kim, M.; Lee, J. H.; Nam, J. M. Plasmonic Photothermal Nanoparticles for Biomedical Applications. *Adv. Sci.* **2019**, *6* (17), 1900471.

(18) Cui, X.; Ruan, Q.; Zhuo, X.; Xia, X.; Hu, J.; Fu, R.; Li, Y.; Wang, J.; Xu, H. Photothermal Nanomaterials: A Powerful Light-to-Heat Converter. *Chem. Rev.* **2023**, *123* (11), 6891−6952.

(19) Xu, C.; Pu, K. Second Near-Infrared Photothermal Materials for Combinational Nanotheranostics. *Chem. Soc. Rev.* **2021**, *50*, 1111−1137.

(20) Jauffred, L.; Samadi, A.; Klingberg, H.; Bendix, P. M.; Oddershede, L. B. Plasmonic Heating of Nanostructures. *Chem. Rev.* **2019**, *119*, 8087−8130.

(21) Yang, B.; Li, C.; Wang, Z.; Dai, Q. Thermoplasmonics in Solar Energy Conversion: Materials, Nanostructured Designs, and Applications. *Adv. Mater.* **2022**, *34*, 2107351.

(22) Sarkar, A. N.; Padhi, S.; Kumari, S.; Jagadevan, S.; Pal, S. Facile Synthesis of Carbon Dot Deposited γ-FeOOH Nanosheet/Poly-pyrrole Composite: A Robust Photocatalyst for Degradation of Antibiotics under Sunlight Irradiation with Enhanced Antibacterial Activity. *Ind. Eng. Chem. Res.* **2023**, *62*, 1227−1244.

(23) Kim, J. T.; Kwon, J.; Lee, H.; Kim, C.; Yang, G. G.; San Lee, G.; Lee, C. W.; Kim, J. G.; Cha, S.; Jung, H. T.; Padmajan Sasikala, S.; Kim, S. O. Sunlight-Driven Self-Cleaning Ultrafine Particulate Matter Filter with Antibacterial Activity. *ACS Nano* **2024**, *18* (8), 6387−6397.

(24) Pramanik, A.; Dhar, J. A.; Banerjee, R.; Davis, M.; Gates, K.; Nie, J.; Davis, D.; Han, F. X.; Ray, P. C. WO3 Nanowire-Attached Reduced Graphene Oxide-Based 1D−2D Heterostructures for Near-Infrared Light-Driven Synergistic Photocatalytic and Photothermal Inactivation of Multidrug-Resistant Superbugs. *ACS Appl. Bio Mater.* **2023**, *6* (2), 919−931.

(25) Gao, Y.; Pramanik, A.; Patibandla, S.; Gates, K.; Hill, G.; Ignatius, A.; Ray, P. C. Development of Human Host Defense Antimicrobial Peptide-Conjugated Biochar Nanocomposites for Combating Broad-Spectrum Superbugs. *ACS Appl. Bio Mater.* **2020**, *3*, 7696−7705.

(26) Begum, S.; Pramanik, A.; Gates, K.; Gao, Y.; Ray, P. C. Antimicrobial Peptide-Conjugated MoS2-Based Nanoplatform for Multimodal Synergistic Inactivation of Bacteria. *ACS Appl. Bio Mater.* **2019**, *2*, 769−776.

(27) Yu, Z. H.; Li, X.; Xu, F.; Hu, X. L.; Yan, J.; Kwon, N.; Chen, G. R.; Tang, T.; Dong, X.; Mai, Y.; Chen, D.; Yoon, J.; He, X. P.; Tian, H. A Supramolecular-Based Dual-Wavelength Phototherapeutic Agent with Broad-Spectrum Antimicrobial Activity Against Drug Resistant Bacteria. *Angew. Chem., Int. Ed.* **2020**, *59* (9), 3658−3664.

(28) Pramanik, A.; Gates, K.; Gao, Y.; Zhang, Q.; Han, F. X.; Begum, S.; Rightsell, C.; Sardar, D.; Ray, P. C. Composites Composed of Polydopamine Nanoparticles, Graphene Oxide, and ε-Poly-l-lysine for Removal of Waterborne Contaminants and Eradication of Superbugs. *ACS Appl. Nano Mater.* **2019**, *2*, 3339−3347.

(29) Xia, P.; Cao, S.; Zhu, B.; Liu, M.; Shi, M.; Yu, J.; Zhang, Y. Designing A 0D/2D S-Scheme Heterojunction Over Polymeric Carbon Nitride for Visible-Light Photocatalytic Inactivation of Bacteria. *Angew. Chem., Int. Ed.* **2020**, *59* (13), 5218−5225.

(30) Duan, G.; Chen, L.; Jing, Z.; De Luna, P.; Wen, L.; Zhang, L.; Zhao, L.; Xu, J.; Li, Z.; Yang, Z.; Zhou, R. Robust antibacterial activity of tungsten oxide (WO$_{3−x}$) nanodots. *Chem. Res. Toxicol.* **2019**, *32*, 1357−1366.

(31) Sankar, M.; He, Q.; Engel, R. V.; Sainna, M. A.; Logsdail, A. J.; Roldan, A.; Willock, D. J.; Agarwal, N.; Kiely, C. J.; Hutchings, G. J. Role of the Support in Gold-Containing Nanoparticles as Heterogeneous Catalysts. *Chem. Rev.* **2020**, *120*, 3890−3938.

(32) Xie, C.; Niu, Z.; Kim, D.; Li, M.; Yang, P. Surface and Interface Control in Nanoparticle Catalysis. *Chem. Rev.* **2020**, *120*, 1184−1249.

(33) Liu, G. N.; Lou, Y. B.; Zhao, Y. X.; Burda, C. Directional Damping of Plasmons at Metal-Semiconductor Interfaces. *Acc. Chem. Res.* **2022**, *55*, 1845−1856.

(34) Sayed, M.; Yu, J. G.; Liu, G.; Jaroniec, M. Non-Noble Plasmonic Metal-Based Photocatalysts. *Chem. Rev.* **2022**, *122*, 10484−10537.

(35) Zhang, Y.; He, S.; Guo, W.; Hu, Y.; Huang, J.; Mulcahy, J. R.; Wei, W. D. Surface-Plasmon-Driven Hot Electron Photochemistry. *Chem. Rev.* **2018**, *118*, 2927−2954.

(36) Villegas, C. E. P.; Leite, M. S.; Marini, A.; Rocha, A. R. Efficient Hot-Carrier Dynamics in near-Infrared Photocatalytic Metals. *Phys. Rev. B* **2022**, *105* (16), 165109.

(37) Paik, T.; Cargnello, M.; Gordon, T. R.; Zhang, S.; Yun, H.; Lee, J. D.; Woo, H. Y.; Oh, S. J.; Kagan, C. R.; Fornasiero, P.; Murray, C. B. Photocatalytic Hydrogen Evolution from Sub stoichiometric Colloidal WO_{3-x} Nanowires. *ACS Energy Lett.* **2018**, *3*, 1904−1910.

(38) Tang, H.; Tang, Z.; Bright, J.; Liu, B.; Wang, X.; Meng, G.; Wu, N. Visible-Light Localized Surface Plasmon Resonance of WO_{3-x} Nanosheets and Its Photocatalysis Driven by Plasmonic Hot Carriers. *ACS Sustain. Chem. Eng.* **2021**, *9*, 1500−1508.

(39) Zeng, J.; Li, Z.; Jiang, H.; Wang, X. Progress on photocatalytic semiconductor hybrids for bacterial inactivation. *Mater. Horiz.* **2021**, *8*, 2964−3008.

(40) Nayak, A. K.; Das, A. K.; Pradhan, D. High Performance Solid-State Asymmetric Supercapacitor Using Green Synthesized Graphene-WO_3 Nanowires Nanocomposite. *ACS Sustain. Chem. Eng.* **2017**, *5*, 10128−10138.

(41) Lin, R.; Wan, J.; Xiong, Y.; Wu, K.; Cheong, W.; Zhou, G.; Wang, D.; Peng, Q.; Chen, C.; Li, Y. A. Quantitative Study of Charge Carrier Dynamics in Well-defined WO_3 Nanowires and Nanosheets: Insight into the Crystal Facet Effect in Photocatalysis. *J. Am. Chem. Soc.* **2018**, *140*, 9078−9082.

(42) Vangara, A.; Pramanik, A.; Gao, Y.; Gates, K.; Begum, S.; Chandra Ray, P. Fluorescence Resonance Energy Transfer Based Highly Efficient Theranostic Nanoplatform for Two-Photon Bioimaging and Two-Photon Excited Photodynamic Therapy of Multiple Drug Resistance Bacteria. *ACS Appl. Bio Mater.* **2018**, *1*, 298−309.

(43) Gu, C.; Wang, Z.; Pan, Y.; Zhu, S.; Gu, Z. Tungsten-based Nanomaterials in the Biomedical Field: A Bibliometric Analysis of Research Progress and Prospects. *Adv. Mater.* **2022**, *35*, 2204397.

(44) Zhang, R.; Song, C.; Kou, M.; Yin, P.; Jin, X.; Wang, L.; Deng, Y.; Wang, B.; Xia, D.; Wong, P. K.; Ye, L. Sterilization of Escherichia coli by photothermal synergy of WO_{3-x}/C nanosheet under infrared light irradiation. *Environ. Sci. Technol.* **2020**, *54*, 3691−3701.

(45) Zhou, Z.; Li, B.; Liu, X.; Li, Z.; Zhu, S.; Liang, Y.; Cui, Z.; Wu, S. Recent Progress in Photocatalytic Antibacterial. *ACS Appl. Bio Mater.* **2021**, *4*, 3909−3936.

(46) Ran, Bi.; Wang, Z.; Cai, W.; Ran, L.; Xia, W.; Liu, W.; Peng, X. Organic Photo-antimicrobials: Principles, Molecule Design, and Applications. *J. Am. Chem. Soc.* **2021**, *143*, 17891−17909.

(47) Xu, J.; Liu, N.; Wu, D.; Gao, Z.; Song, Y. Y.; Schmuki, P. Upconversion Nanoparticle-Assisted Payload Delivery from TiO_2 under Near-Infrared Light Irradiation for Bacterial Inactivation. *ACS Nano* **2020**, *14*, 337−346.

(48) Yang, Y.; Yin, H.; Li, H.; Zou, Q.; Zhang, Z.; Pei, W.; Luo, L.; Huo, Y.; Li, H. Synergistic Photocatalytic-Photothermal Contribution to Antibacterial Activity in BiOI-Graphene Oxide Nanocomposites. *ACS Appl. Bio Mater.* **2018**, *1* (6), 2141−2152.

(49) Fan, Z.; Shelton, M.; Singh, A. K.; Senapati, D.; Khan, S. A.; Ray, P. C. Multifunctional Plasmonic Shell−Magnetic Core Nanoparticles for Targeted Diagnostics, Isolation, and Photothermal Destruction of Tumor Cells. *ACS Nano* **2012**, *6*, 1065−1073.

(50) Dai, X.; Fan, Z.; Lu, Y.; Ray, P. C. Multifunctional Nanoplatforms for Targeted Multidrug-Resistant-Bacteria Theranostic Applications. *ACS Appl. Mater. Interfaces* **2013**, *5*, 11348−11354.

(51) Baffou, G.; Cichos, F.; Quidant, R. Applications and Challenges of Thermo-plasmonics. *Nat. Mater.* **2020**, *19*, 946−958.